nature sustainability

Article

https://doi.org/10.1038/s41893-022-01023-2

Dynamic electrochromism for all-season radiative thermoregulation

Received: 1 July 2022

Accepted: 16 November 2022

Published online: 26 January 2023

Check for updates

Chenxi Sui[1,2], Jiankun Pu[3], Ting-Hsuan Chen[2], Jiawei Liang[2], Yi-Ting Lai[2,4], Yunfei Rao[2,5], Ronghui Wu[1], Yu Han[1], Keyu Wang[2], Xiuqiang Li[2,6], Venkatasubramanian Viswanathan[3] ✉ & Po-Chun Hsu[1,2] ✉

Radiative thermoregulation can reduce the energy consumption for heating, ventilation and air-conditioning (HVAC) in buildings, and therefore contribute substantially to climate change mitigation. Electrochromism, a phenomenon in which a material exhibits reversible colour changes under an external electrical stimulus, can help control the heat balance of buildings in response to fluctuating weather conditions; however, its implementation has been largely limited to visible and near-infrared wavelength regimes. Here we develop an aqueous flexible electrochromic design for use as a building envelop based on graphene ultra-wideband transparent conductive electrode and reversible copper electrodeposition, in which the thermal emissivity can be tailored to vary between 0.07 and 0.92 with excellent long-term durability. Building energy simulations show that our design as building envelopes can save on year-round operational HVAC energy consumption across the United States by up to 43.1 MBtu on average in specific zones. Such dynamic emissivity tunability can further serve as a non-destructive technological solution to retrofit poorly insulated or historic buildings. Our work suggests a feasible pathway to radiative thermoregulation for more energy-efficient HVAC and solving some of the global climate change issues.

Buildings account for as high as 30% of global energy consumption and emit 10% of global greenhouse gas, which causes environmental and economic challenges for a sustainable future[1–4]. Of such colossal energy consumption, approximately 48% is for space heating and cooling alone[5], calling for innovation to sustainably manage building temperature and create net-zero-energy buildings. Radiative cooling materials have been developed to provide an effective approach to utilizing the coldness of outer space[6–8] to save on air-conditioning energy consumption of buildings during the hot summer. Apart from supplying cooling power to cool buildings, low-emissivity (low-ε) building envelopes can also reduce heating, ventilation and air-conditioning (HVAC) energy consumption by suppressing radiative heat loss in cold climates[9,10]. However, the applicability of the above-mentioned roof/wall envelopes with static radiative properties is restricted by the spatially and temporally variable weather[5]. Additionally, global warming causes increasingly frequent extreme weather events[11], urgently demanding smarter and wider adaptability to different weather conditions for buildings. A promising future net-zero-energy building should be able to dynamically tune its thermal emissivity in accordance with the weather conditions and occupants' demands[12]. To provide buildings with weather adaptability, thermochromic materials have been demonstrated to vary the solar and/or mid-infrared radiative properties in response

[1]Pritzker School of Molecular Engineering, University of Chicago, Chicago, IL, USA. [2]Thomas Lord Department of Mechanical Engineering and Materials Science, Duke University, Durham, NC, USA. [3]Department of Mechanical Engineering, Carnegie Mellon University, Pittsburgh, PA, USA. [4]Department of Materials Engineering, Ming Chi University of Technology, New Taipei City, Taiwan. [5]Zhejiang Provincial Key Laboratory of Fiber Materials and Manufacturing Technology, Zhejiang Sci-Tech University, Hangzhou, China. [6]Institute for Frontier Science, Nanjing University of Aeronautics and Astronautics, Nanjing, China. ✉e-mail: venkvis@cmu.edu; pochunhsu@uchicago.edu

to the weather conditions, showing promising energy saving potential and functionality[13–16]. The tuning criterion is a fixed phase change temperature, and it would be a step further to develop dynamically on-demand programmable radiative thermoregulation. Mechanical methods[5,17,18] have been demonstrated to dynamically switch between solar heating and radiative cooling, but the requirement of mechanical moving parts inevitably results in challenges in wide deployment, such as in transportation, storage and installation.

Electrochromic devices can dynamically manage buildings' optical and thermal properties without mechanical force. Substantial progress has been made in both fundamental electrochemistry and commercialization[19–29]. However, it is still challenging to realize large mid-infrared (mid-IR) emissivity tuning contrast and long-term durability. In addition, for building applications, the use of costly and flammable electrolytes limits scalability and creates safety concerns[26]. Indeed, creating energy-efficient, durable and electrically switchable building envelopes for radiative thermal management requires a rational systematic design of electrochemical redox reactions, electrolyte and electrode materials.

Here, to tackle the bottleneck, we design a copper (Cu)-based aqueous electrochromic mid-IR building envelope. The adoption of aqueous cupric solution makes the electrochromic device non-flammable, and using the ultra-wideband transparent conductive electrode allows considerable dynamic range of thermal emissivity tunability from 0.07 to 0.92. The switching is stable, non-volatile, efficient and mechanically flexible. After 1,800 deposition-stripping cycles, the emissivity contrast only reduces by 21%. The density functional theory (DFT) calculations confirm the uniform and durable deposition of Cu on the platinum (Pt)-modified electrode. Finally, the rigorous building energy calculations show that our aqueous dynamic building envelope can save 8.4% of US buildings' HVAC energy consumption on average among climate zones 5–8 in the United States (see definition in Supplementary Fig. 1)[30].

Results

Aqueous electrolyte for electrochromism

As shown in Fig. 1a, the electrochromic device contains a Pt-modified ultra-wideband transparent electrode as the working electrode, which is made of polyethylene, gold grid, monolayer graphene and 2 nm sputtered Pt, Cu foil as the counter electrode and aqueous electrolyte. The Pt-modified ultra-wideband transparent conductive electrode is optimized to maintain low mid-IR reflectivity (Supplementary Figs. 2–4). Because of the underlying high-emissivity electrolyte, both transmission and absorption of the transparent electrode will result in emission, so the low reflectivity of the Pt-modified ultra-wideband transparent conductive electrode and the high IR-absorbing electrolyte deliver the high emissivity at the stripping state (pristine or +1 V bias versus Cu foil), leading to a cooling state that enhances the radiative heat exchange between the buildings and the outer space through the atmospheric transparent window. When the Cu is gradually deposited onto the top transparent electrode (−0.7 V versus Cu foil), the Cu nanoparticles grow larger and denser on the Pt-modified graphene, making the whole metal layer thicker and denser. Thus, the metal layer would become more IR-reflective, which contributes to the low-ε heating state, thereby suppressing radiative heat loss. When the device switches states, the visible appearance of the device also changes. The original device shows dark white (the colour of the porous nylon separator soaked with the electrolyte) at the high-ε state and copper at the low-ε state because the polyethylene film on the top is transparent. This varying visible appearance might be undesirable for some users, but the issue can be solved by covering the device with mid-infrared transparent pigment without affecting emissivity tunability (Supplementary Figs. 5–8).

The Cu-aqueous electrolyte possesses three advantages for large-scale applicability: (1) non-flammability, (2) lower price and (3) outstanding electrochromic performance. Different from water, the commonly used dimethyl sulfoxide (DMSO) solvent in silver electrodeposition has some safety concerns. DMSO is combustible and its auto-ignition temperature is 300 °C[31]. Additionally, when DMSO is heated up, it will quickly decompose into sulfur dioxide[31]. DMSO also rapidly diffuses into the skin, which enhances the absorption of other toxic chemicals[31]. To this end, a flammability test was conducted to examine the safety of the Cu-aqueous electrolyte compared to the Ag-DMSO electrolyte that has been used for mid-IR tuning in previous reports[19,26] (Fig. 1b). Combustion occurred when the Ag-DMSO electrolyte was exposed to fire, confirming the better safety of Cu-aqueous electrolyte. More detailed combustion experiments are shown in Supplementary Fig. 9. Given the flammability of DMSO, the combustion of DMSO would travel in the whole dynamic emissivity of buildings with DMSO if one corner of the device were on fire. It is worth mentioning that the Cu-aqueous electrolyte is 79.3% cheaper than the Ag-DMSO electrolyte due to the lower cost of solvent and metal salt, as shown in Supplementary Fig. 10.

Non-volatile switching is another key criterion for smart building envelopes. Previous reports on the Ag-DMSO electrolyte system[19,26] require supplying a small bias to maintain the deposited (low-ε) state, due to the excessive bromide and silver-bromide complex ions. This self-dissolution can lead to considerably low tuning efficiency at the low-ε state because of the excessive electricity consumed to compensate for the loss of metal film. Recent research has already started to solve this issue and indeed realized the non-volatile electrodeposition by fixing a silver layer on the counter electrode as the charge mediator, further promoting the applicability of the Ag-DMSO electrolyte[32]. In contrast, the Cu-aqueous electrolyte can bypass this limitation by using the Cu^{2+}/Cu (metal film) rather than Br^{3-}/Br^{-} as the counter electrode redox couple. In Fig. 1c, 400 s negative bias of −0.7 V and −1.5 V were respectively applied on the electrochromic devices with Cu-aqueous and Ag-DMSO electrolyte and the device subsequently left at open-circuit. The as-deposited Ag film with the Ag-DMSO electrolyte quickly dissolved back into the electrolyte in only 100 s; in contrast, the as-deposited Cu film stayed for more than 5.5 h in the Cu-aqueous electrolyte, as confirmed by the stable low emissivity. Such a non-volatile electrodeposition also allows the emissivity to be varied at different values and kept without energy consumption (Supplementary Fig. 11).

To achieve effective thermal management through mid-IR modulation, an electrochromic device needs to perform the tunability in an extensive mid-IR range. Thanks to the high transmission of the graphene-based ultra-wideband transparent conductive electrode, the device can switch between the heating (low-ε) and cooling (high-ε) modes by depositing and dissolving the Cu film. Figure 1d shows the Fourier-transform infrared spectroscopy (FTIR) of the device at two states. The building envelopes can switch between cooling mode ($\varepsilon_{7.5-13\mu m} \approx 0.92$) and heating mode ($\varepsilon_{7.5-13\mu m} \approx 0.07$). The thermal emissivity contrast of $\Delta\varepsilon \approx 0.85$ is the highest among the reported non-mechanical mid-IR switching devices, including both thermochromic and electrochromic devices[14–16,19,22,27,29] (Fig. 1e). More detailed comparison is shown in Supplementary Table 1.

The above results allow us to safely assume that the electrical energy consumption to maintain the emissivity states is negligible, and calculate the required annual electricity to switch the entire building envelope, as shown in Fig. 1f. The calculation method is described in Supplementary Note 1. The result shows that, even under the conservative assumption that the building envelope is switched three times a day with a large emissivity contrast of 0.80, the required annual electricity is negligible (only 0.18%) compared with the annual electricity usage of a baseline residential building[33].

Reversibility of the Cu electrodeposition

To further investigate the emissivity tuning mechanism, scanning electron microscopy (SEM) and energy-dispersive X-ray spectroscopy (EDX) were used to characterize the surface morphology and elemental composition of the electrodeposited metal film (Fig. 2a). Results show

https://doi.org/10.1038/s41893-022-01023-2

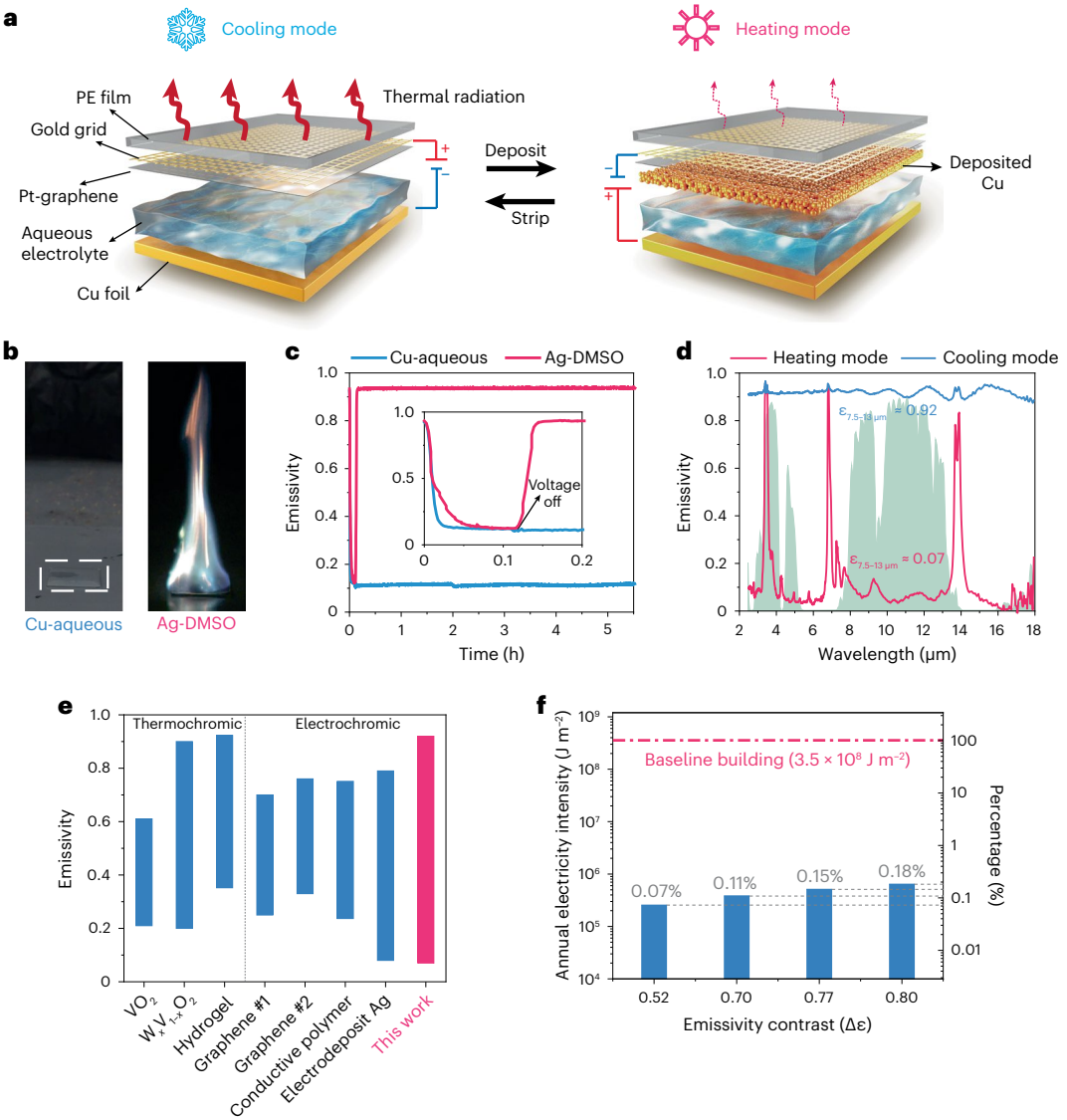

Fig. 1 | Concept and advantages of the electrochromic mid-IR modulation system with an aqueous electrolyte. a, Schematic demonstration of the electrochromic system. The device can be tuned between the heating mode (Cu-deposited, right) and the cooling mode (Cu-stripped, left). **b**, Flammability test of Cu-aqueous (left) and Ag-DMSO (right) electrolyte. **c**, Non-volatility test of heating mode (metal-coated). $\lambda = 10$ μm. **d**, FTIR spectra for the heating and cooling modes. The green shaded area is the atmospheric transparent window. **e**, Comparison of tunable emissivity contrast with different strategies: thermochromic VO_2[14], thermochromic $W_xV_{1-x}O_2$[15], thermochromic hydrogel[16], electrochromic graphene devices #1[29] and #2[27], electrochromic conductive polymer devices[22] and reversible electrodeposited Ag device[19]. **f**, Annual electricity consumption for an aqueous device switching to different emissivity. The red dashed line represents the annual electricity usage of a baseline building[33]. The annual electricity consumption of the device switching to different emissivity states as a percentage of the annual electricity usage of a baseline building is indicated on the bar.

that Cu can be deposited uniformly due to the introduction of the Pt modification and polymer inhibitor[26,28]. The composition of the deposited metal film was characterized by X-ray photoelectron spectroscopy (XPS) and X-ray diffraction (XRD). In Fig. 2b, the peaks at 932.5 and 952.5 eV in the Cu 2p scan confirm the existence of the metallic Cu(0). The shifted Cu $2p_{3/2}$ peak at 934.5 eV and the satellite around 944 eV correspond to the small amount of CuO[34]. Composition analysis of Cu shows that there is 25.11% CuO. After electrodeposition, XRD analyses reveal peaks at 43.4° and 50.5° appearing on the ultra-wideband transparent electrode, which can be assigned to Cu (111) and Cu (200)[35,36], as shown in Fig. 2c. There is no signal for the crystallized CuO in the XRD data. Since the XPS analyses the top surface layer of the sample and XRD delivers the much deeper measurement, we inferred that the CuO only exists in the top surface layer, which elucidates that the metallic Cu dominates the electrodeposition process and results in low emissivity.

Figure 2d,e show the cycle test of the mid-IR emissivity tuning. The large emissivity contrast can be maintained for 1,000 cycles and only degrade 21% after 1,800 cycles, which represents a significant improvement from the previous reports using Ag-DMSO electrolyte (only up to 300–400 cycles)[19,26]. The emissivity spectra maintain their broadband feature after 2,500 cycles (Fig. 2e). It is noteworthy that the heating mode (low-ε state) degrades faster than the cooling mode (high-ε state), which could be attributed to the irrecoverable absorption of Cl^- ions on the working electrode and the oxidation of the metal film[24,26]. It should be mentioned that the deposition and stripping potentials were carefully selected to avoid hydrogen and oxygen evolution reactions[24] (Supplementary Figs. 12 and 13).

https://doi.org/10.1038/s41893-022-01023-2

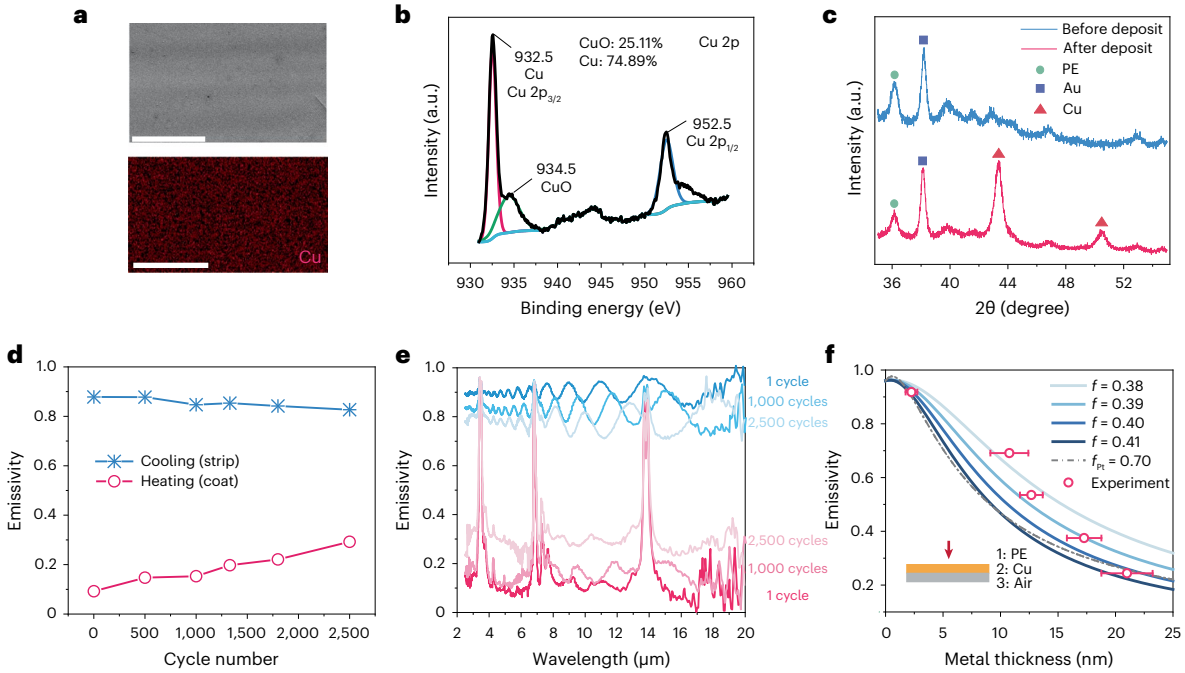

Fig. 2 | Elementary and mid-IR tunability analysis. a, SEM image and EDX mapping of the deposited film. Scale bar, 50 μm. **b**,**c**, XPS (**b**) and XRD (**c**) analyses of the deposited film. **d**, Cycle life test of the electrochromic mid-IR system. **e**, FTIR spectra for different cycle numbers. **f**, Relationship between emissivity and the thickness of the as-deposited metal film. EMT was used to fit the relationship to physically explain the mid-IR tunability. The emissivity was both measured and calculated under $\lambda = 10$ μm. Inset: schematic demonstration of the electromagnetic wave propagating through the stratified medium. The sample size for deriving the statistics is 5 and the error bars represent mean ± s.d.

To quantitively explain the monotonic trend of the decreased emissivity with the increased amount of electrodeposited Cu, we adopted the effective medium theory (EMT) to fit the experimental results and obtain the relationship between emissivity and Cu film thickness with different volume fractions (Fig. 2f), given the porous nature of the Cu nanoparticle film and the large dimensional mismatch between the nanoparticles and thermal radiation wavelength. The effective permittivity $\tilde{\varepsilon}_{\mathrm{eff}}$ of the porous Cu film was calculated using Bruggeman's EMT (equation 1)[37]:

$$f\frac{\tilde{\varepsilon}_{\mathrm{Cu}}-\tilde{\varepsilon}_{\mathrm{eff}}}{\tilde{\varepsilon}_{\mathrm{Cu}}+2\tilde{\varepsilon}_{\mathrm{eff}}}+(1-f)\frac{\tilde{\varepsilon}_{\mathrm{air}}-\tilde{\varepsilon}_{\mathrm{eff}}}{\tilde{\varepsilon}_{\mathrm{air}}+2\tilde{\varepsilon}_{\mathrm{eff}}}=0 \quad (1)$$

where f is the volume fraction of the Cu nanoparticles, and $\tilde{\varepsilon}_{\mathrm{Cu}}$ and $\tilde{\varepsilon}_{\mathrm{air}}$ are the wavelength-dependent permittivities of Cu and air, respectively. Note that we used air rather than aqueous electrolyte for calculation because the empirical data were measured ex situ in the dry state. Then, considering three stratified media (inset of Fig. 2f), the thickness-dependent reflectivity $\mathcal{R}$ of the porous Cu film was obtained (equation 2)[38,39]:

$$\mathcal{R}=\left|\frac{r_{12}+r_{23}e^{2i\beta}}{1+r_{12}r_{23}e^{2i\beta}}\right|^2 \quad (2)$$

where $r_{\mathrm{mn}}=(n_{\mathrm{m}}\cos\theta_{\mathrm{m}}-n_{\mathrm{n}}\cos\theta_{\mathrm{n}})/(n_{\mathrm{m}}\cos\theta_{\mathrm{m}}+n_{\mathrm{n}}\cos\theta_{\mathrm{n}})$, $\beta=(\frac{2\pi}{\lambda})n_2h\cos\theta_2$, $n_{\mathrm{m}}=\sqrt{\tilde{\varepsilon}_{\mathrm{m}}}$, and $\theta_{\mathrm{m}}=\sin^{-1}\left(\frac{n_1\sin\theta_1}{n_{\mathrm{m}}}\right)$. θ, n and h are the incident angle, refractive index and thickness of the porous Cu film, respectively. m and n refer to the indices of different layers (1, 2, and 3). Medium 1 and 3 are polyethylene and air, and medium 2 corresponds to the porous Cu film. e and i are the Euler's number (≈2.71828) and imaginary unit, respectively. Finally, the emissivity was calculated using $1-\mathcal{R}$ based on Kirchhoff's radiation law. As shown in Fig. 2f, the experimental results (red circles) are consistent with the theoretical calculations (blue lines) when varying the volume fraction between 0.38 and 0.41. It should be noted that the initial data point for no Cu deposition was approximated by replacing the permittivity of the Cu ($\tilde{\varepsilon}_{\mathrm{Cu}}$) with that of Pt ($\tilde{\varepsilon}_{\mathrm{Pt}}$) in equation (1). The result shows that the initial Pt volume fraction f_{Pt} is about 0.70. The structure of this nanoscopic Pt is shown in the TEM image (Supplementary Fig. 16). When the Cu starts to deposit, the volume fraction decreases to below 0.38, and the thickness of the deposited metal layer increases to around 11 nm due to the sparsely packed Cu nanoparticles. As more Cu deposits, the volume fraction increases together with the thickness, indicating that the Cu nanoparticles have become larger and denser, blocking thermal radiation.

Pt modification for uniform electrodeposition

As stated in the previous research, the Pt-nanoparticles modification on the working electrode can enhance the uniformity and durability of the reversible metal electrodeposition[19,24,26]. On the bare graphene substrate, Cu tends to become sparsely distributed large particles (Fig. 3a). According to EMT[37], the metal film must be dense and continuous enough to reach the percolation threshold that can behave metal-like in optics (reflecting the electromagnetic wave). As shown in Fig. 3b, with the same charge density of electrodeposition (0.175 C cm^{-2}), the Cu film grown on the Pt-modified surface possesses lower emissivity, contributing to a more considerable contrast in the mid-IR range.

To realize the fundamental difference between the bare graphene and Pt-modified graphene for Cu electrodeposition, we further studied the heterogeneous interaction of the Cu atoms with different substrates using DFT. Adsorption free energy between substrates and Cu atoms and interaction energy between Cu-Cu adatoms are two factors to characterize the heterogeneous nucleation of Cu[40]. Three different systems were simulated for comprehensive study (Fig. 3c). To evaluate the adsorption energy, we considered the following reaction

https://doi.org/10.1038/s41893-022-01023-2

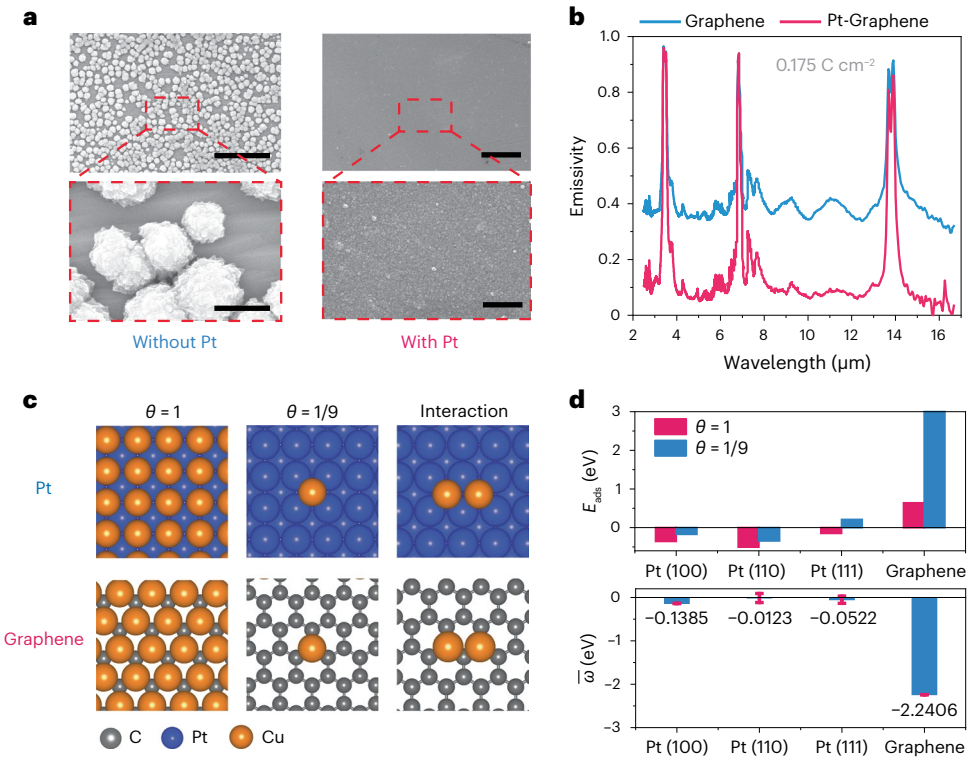

Fig. 3 | Characterization and theoretical explanation of the performance enhancement by Pt modification. a, SEM images of the deposited Cu morphology on the transparent electrode with and without Pt modification. Scale bars, 10 μm (low magnification, top) and 1 μm (high magnification, bottom). **b**, FTIR spectra of the Cu films deposited on the bare and Pt-modified graphene transparent electrode. Both samples were coated with the same charge density of 0.175 C cm^{-2}. **c**, Atomic diagrams for DFT calculation. **d**, Calculated adsorption energy (top) between substrates (Pt or graphene) and Cu atom, and the interaction energy (bottom) between two adjacent Cu atoms on different substrates. Error bars represent mean ± s.d.

mechanism, and calculated the initial electrochemical adsorption step as:

$$Cu^{2+}_{(sol)} + 2e^- + * \rightleftharpoons Cu^* \quad (3)$$

where * refers to an adsorption site on the bare graphene and Pt substrates. Using the computational Cu electrode reference, the adsorption energy $\left(E^{\theta}_{ads}\right)$ can then be described as:

$$E^{\theta}_{ads} = \Delta G_{Cu^*} - \Delta G_{Cu} \quad (4)$$

where θ is the coverage factor, ΔG_{Cu^*} is the Gibbs free energy of the Cu adatom and ΔG_{Cu} is the Gibbs free energy of the bulk Cu. We approximate the free energies to be equal to their DFT energies, neglecting entropic contributions:

$$E^{\theta}_{ads} = (E^{\theta}_{slab} - E^{clean}_{slab}) - E^{bulk}_{Cu} \quad (5)$$

where E^{θ}_{slab} is the DFT energy of the substrate with Cu adatom, E^{clean}_{slab} is the DFT energy of the pure substrate and E^{bulk}_{Cu} is the DFT energy of the bulk Cu. Both adsorption energies of Cu to graphene and Pt were calculated at high coverage ($\theta = 1$) and low coverage ($\theta = \frac{1}{9}$)[41]. In addition, all low index surfaces of Pt were considered for the calculation. Details of the calculation and computation setup are described in Methods. In the top plot of Fig. 3d, a decrease in adsorption energy from low to high coverage can be observed across all the systems, indicating that the Cu adatom would adsorb on Pt and graphene surfaces after overcoming the initial nucleation overpotential. The results show that the adsorption energies of the Cu adatom on graphene at high and low coverage are both positive, that is, 0.98 eV and 3.10 eV, respectively, much higher than those on Pt surfaces. The Cu adatom would have weak interaction with graphene and would prefer to cluster rather than form uniform films on the graphene surface. To verify that Cu indeed has a higher tendency to cluster on graphene surface, the interaction energy ω between adatoms was calculated using:

$$\omega = E^{2Cu}_{slab} - \left(2 * \left(E^{clean}_{slab} + E^{bulk}_{Cu}\right) + E^{low\theta}_{ads}\right) \quad (6)$$

where E^{2Cu}_{slab} is the DFT calculated energy of a substrate with 2 Cu atoms and $E^{low\theta}_{ads}$ is the adsorption energy of Cu at low coverage. Thus, the interaction energy is the direct measurement of the binding energy of two Cu adatoms on a given substrate, as shown in the right panel of Fig. 3c. The mean and the standard deviation of the interaction energy of different directions were calculated. The mean interaction energy of Cu adatoms on bare graphene substrate is ~2.17 eV lower than that on Pt substrate. This indicates that Cu prefers to nucleate around the random-distributed defects, causing the discrete, sparse clusters of the Cu particles on the bare graphene substrate. The defects or edges of the graphene tend to attract metal/metal oxide atoms, which might result from its dangling bonds or termination by other reactive species[42]. A tight connection between the experiments and simulations confirms the benefit of Pt modification for uniform electrodeposition.

Energy-efficient building envelope application

The high-performance mid-IR electrochromism, non-flammability and flexibility (Supplementary Figs. 17–19) of the Cu-aqueous mid-IR modulation device allow the application of smart building envelopes for thermal management by electrical bias (Fig. 4a). To experimentally demonstrate such applicability, we attached the electrochromic device onto a heater and measured the heat loss through the device under

https://doi.org/10.1038/s41893-022-01023-2

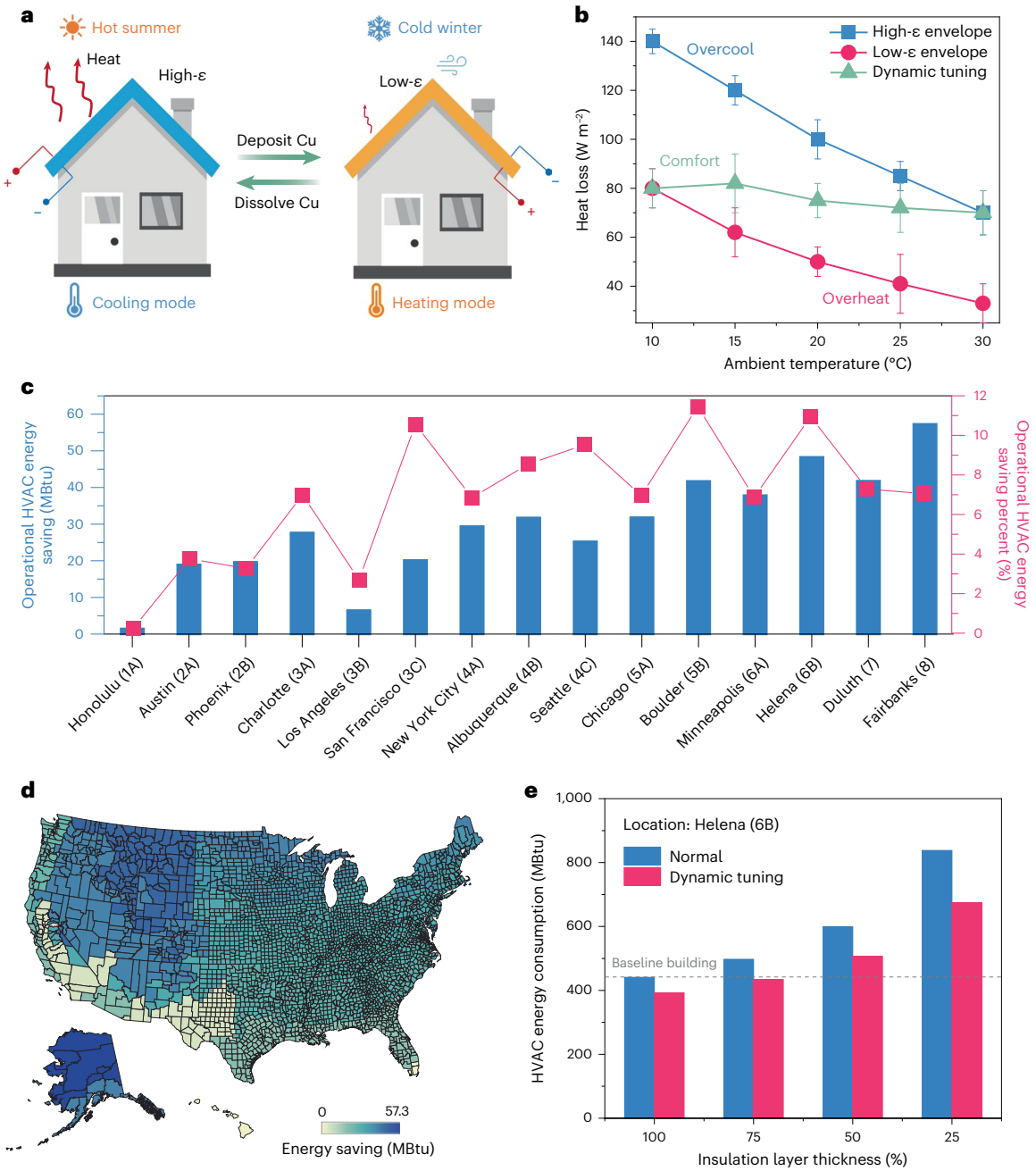

Fig. 4 | Smart building envelope for all-season energy saving application. **a**, Scheme for smart building envelope with radiative thermal management. By continuously tuning the emissivity, the building can maintain thermal comfort efficiently in all seasons. **b**, Heat loss of building surfaces with different envelopes under different ambient temperatures. The sample size for deriving the statistics is 5 and error bars represent mean ± s.d. **c**, Year-round operational HVAC energy saving and saving percentage of buildings enveloped with the electrochromic device. **d**, Energy saving map of the building envelope by the electrochromic device for all 15 climate zones in the United States. **e**, HVAC energy consumptions for different thermal insulated buildings with/without dynamic emissivity envelopes installed.

different ambient temperatures (Fig. 4b). Detailed experimental design is shown in Methods (Supplementary Fig. 20). Without the ability to change the emissivity, the high-ε/low-ε building envelope tends to overcool/overheat the building in a cold/hot environment, as confirmed by the high/low heat loss (over 100 W m^{-2} or below 50 W m^{-2}). In contrast, the electrochromic device can vary its emissivity in response to different ambient temperatures to maintain a constant heat loss (near 75 W m^{-2}) for the thermal comfort of the buildings.

To comprehensively demonstrate building HVAC energy saving ability, the remarkable optical properties of the Cu-aqueous electrochromic device were imported into EnergyPlus as the emissivity of buildings' sidewalls and roofs to calculate the year-round energy saving. The calculation was conducted for 15 cities, corresponding to 15 climate zones in the United States (Supplementary Fig. 1)[2,5,30]. In Fig. 4c, we plotted the operational HVAC energy saving and saving percentage of buildings enveloped with the electrochromic device. The results show that most buildings located in weather with high variations, including daily and seasonal fluctuation, require dynamic thermal management. The dynamic emissivity tunability of the device helps the building save more energy compared with the constant low-ε

or high-ε building envelopes (Supplementary Fig. 21). In Fig. 4c,d, the electrochromic device adaptive to the fluctuating weather conditions can achieve higher energy saving, especially in cold areas.

In addition to the operational energy and carbon footprint due to HVAC, the building insulation material is also considered an emission source, known as embodied carbon (Supplementary Fig. 22)[43–45]. Furthermore, some historic buildings with inefficient thermal insulations are not allowed to be structurally intervened[46], so we propose that enveloping the buildings with our dynamic emissivity device can be an instant and non-destructive way to reduce the HVAC energy consumption and operational CO_2 emission of the poorly insulated or historic buildings. In Fig. 4e, we calculated the HVAC energy consumption for different thermal insulated buildings in Helena. The HVAC energy consumption of midrise apartments installed with dynamic emissivity devices increases to 506.86 and 675.14 MBtu when the thickness of the insulation layer is decreased to 50% and 25%, respectively. These two values are already beyond the HVAC energy consumption of the baseline building (440.93 MBtu), which means the device cannot fully compensate for the higher HVAC energy consumption due to the reduced thermal insulation layer. Still, for buildings with a 75% thick layer of insulation, the dynamic thermal emissivity tuning device does help the building decrease its HVAC energy consumption from 497.59 MBtu to 433.69 MBtu (below the value of the baseline building). The above simulation indicates that the device can still reduce energy consumption even using only 75% of thermal insulation materials, so both operational and embodied carbon are saved (Supplementary Fig. 29). In Supplementary Fig. 28, we further show that the dynamic emissivity device helps old/historic buildings save 107.7 MBtu of HVAC energy consumption all year, which is 2.23 times larger than it can save on new construction buildings.

Discussion

This research develops an aqueous electrically switchable electrochromic building envelope for building thermoregulation. First, comprehensive experiments were conducted to demonstrate the benefits of Cu-aqueous electrolytes. The non-flammability of the aqueous electrolyte contributes to a safe building application. By removing the Br^{3-}/Br^{-} redox couple, the metal deposition showed a non-volatile tunability with a 0.85 thermal emissivity contrast with long-term durability. Second, we fundamentally explained the benefit of Pt modification for uniform electrodeposition through various characterization techniques and DFT simulations. Finally, despite the good energy saving capability of thermal insulation materials, our dynamic emissivity device offers a more convenient option for energy-efficient retrofitting compared with the complicated process of installing additional insulation materials into walls and roofs, especially for poorly insulated buildings in cold areas and for historic buildings. It is worthwhile to note that future efforts are needed to reduce the cost of the raw materials and fabrication process to scale up the device. The current limitations and future directions of the electrochromic mid-IR building envelopes (hydrophobic treatment, cost of the device, retrofitting and so on) are analysed in Supplementary Discussion. We hope this work can pave the way for designing sustainable electrochromic devices in thermal emissivity modulation for smart building envelopes and deepen fundamental understanding of reversible metal electrodeposition.

Methods

Electrolyte preparation

The aqueous electrolyte consists of 20 mM $Cu(ClO_4)_2$, 1 M $LiClO_4$, 10 mM $HClO_4$ and 10% (wt.) poly(vinyl alcohol) for uniform electrodeposition. The whole solution was mixed under 80 °C. The DMSO electrolyte was prepared as previously described[26]. The main reason we chose perchlorates in our electrolyte is that perchlorates have been reported to be good anions for aqueous reversible Cu electrodeposition[24]. This is because they avoid the side reaction related to Cu^{+}, which limits the durability of the electrodeposition, compared with chlorides[24]. Also, the perchloric acid does not etch the working electrode (Supplementary Fig. 24). We conducted an analysis of the electrolytes for reversible metal deposition by screening the anions in the electrolyte to show the full possibilities of electrolytes (Supplementary Discussion 5).

Electrochromic building envelope device fabrication

The monolayer chemical vapour deposited graphene on Cu was purchased from Cheap Tube. For the gold (Au) grid fabrication, the photoresist (NFR-016D2) was spin-coated on the graphene and then photolithographed to form microchannels (with width and spacing of 10 μm and 1 mm, respectively). Then, 200 nm Au was evaporated (Kurt J. Lesker PVD 75) and lifted off in acetone to form the Au grid on the graphene. The graphene coated with the Au grid was hot-pressed onto the transparent polyethylene film at 99 °C to ensure strong bonding between the graphene and the polymer (partially melt the polyethylene surface). By doing so, the gold grid would be partially embedded into the polyethylene surface and the graphene would be tightly bonded to polyethylene. Finally, the Cu on the graphene was etched away by iron (III) chloride solution.

To fabricate the whole building envelope device, 2 nm Pt was sputtered onto the transparent conductive electrode, which serves as the working electrode. Although the high-energy plasma and metal sputtering could potentially damage the graphene, we did not observe any negative impact on electrodeposition. Since the metal was only 2 nm thick, the sputtering time was short and the damage to the graphene was not severe. The reversibility of the electrodeposition relies on the conductivity of the transparent electrode and the catalytic effect of the Pt layer (confirmed by our DFT simulation). The sheet resistance of the ultra-wideband transparent conductive electrode before and after Pt sputtering remained stable (~25 Ω $square^{-1}$ and ~20 Ω $square^{-1}$ before and after sputtering). The counter electrode was Cu foil. Two electrodes with the Cu-aqueous electrolyte in between were sandwiched and sealed by acrylic tapes (3M, ~0.25 mm).

Because of the higher conductivity of gold than monolayer graphene, one might presume that Cu would deposit around the Au grid. While it is true that the Au grid has a smaller ohmic loss and higher local deposition rate, the difference was minimized by choosing high-quality graphene and Pt modification, as demonstrated in Supplementary Fig. 23.

Electrochemistry

Electrochromic performance testing was conducted via the VMP3 (BioLogic). For the constant potential electrodeposition process, the deposit potential was −0.6 V (versus Ag/AgCl) for the 3-electrode system and −0.7 V (versus Cu foil) for the 2-electrode device. For the constant potential stripping process, the potential was +0.3 V for the 3-electrode system (versus Ag/AgCl) and +1 V for the 2-electrode system (versus Cu foil). The cyclic voltammetry test was scanned at a rate of 20 mV s^{-1}.

Characterizations

FTIR characterization of the static and real-time spectra was conducted using an iS50 spectrometer (Thermo Fisher) equipped with a diffuse gold integrating sphere. The SEM images and EDX elements of the deposited Cu nanoparticles were analysed using a high-resolution field-emission scanning electron microscope (Apreo S, Thermo Fisher). The XPS spectrum was obtained on the X-Ray Photoelectron spectrometer (Kratos Analytical Axis Ultra). The infrared images were recorded using an IR camera (FLIR E60).

Heat transfer measurement

The heat loss of the building enveloped with the electrochromic device was measured in an acrylic-enclosed chamber with cooling/heating

water recirculation. The setup of this experiment is described in Supplementary Fig. 20. The surface temperature was controlled by the top heater. To eliminate lateral heat loss, the temperature guard heater was heated to have the same temperature as the top heater. Both top and guard heaters were connected to a DC power supply (Rigol, DP821A). The temperatures of the two heaters were measured by two thermal couples, collected by the DAQ module (MC Measurement Computing, USB-2408). Such a process was achieved by the PID control system, coded by LabView. By doing so, the heat was transported vertically in a one-dimensional direction. The building envelop samples, heaters and vacuum insulation panels were attached by thermal paste. The ambient temperature was controlled by recirculating water pipes. To simulate the real building in all seasons, we chose five ambient temperatures: 10 °C, 15 °C, 20 °C, 25 °C and 30 °C. For these ambient temperatures, we set the surface temperature to be 23 °C, 27 °C, 30 °C, 33 °C and 37 °C. Since the building surface temperature was always higher than the ambient temperature, the building would lose heat to the environment. The measurement was conducted under thermal equilibrium (waited 10 min after the initial temperature rise peak), so the heat loss through the building envelope was equal to the power density of the top heater.

Building energy saving calculation

We used EnergyPlus, an open-source whole-building energy simulation software (https://energyplus.net/), to compute the year-round HVAC energy consumption. To simulate a realistic building, EnergyPlus utilizes the heat balance-based solution of all heat transfer effects for both internal and external building surfaces. The software takes all loads (equipment, occupants and lighting) into account on the basis of the occupants' thermal comfort. The governing equation (energy-balanced equation) is solved between internal (room temperature) and external (ambient temperature based on weather data) surfaces hourly for the whole year. The HVAC energy consumption of buildings in different US areas was calculated by EnergyPlus version 9.4. Fifteen cities were selected to represent 15 climate zones in the United States [30]. Here we used hourly weather data for a typical meteorological year (TMY2). The new-2004 midrise apartment model from the US Department of Energy was utilized for simulation. The unit floor space area was 783.75 m^2 and the building was in a rectangular shape (length, 46.33 m; width, 16.91 m; height, 12.19 m) with 4 stories, and the window-to-wall ratio was 15%. The baseline building models were installed with the conventional wall properties (default value as downloaded). The cooling and heating loads were calculated hourly all year round. For the building installed with the electrochromic mid-IR device, the emissivity of the out-layer materials was set to 0.07 and 0.92 for heating and cooling modes, respectively. We used normal buildings (the default building model with emissivity equal to 0.9) to represent the baseline. By running the model for building under cooling and heating modes, the cooling and heating loads under heating and cooling modes can respectively be obtained. $P_{cool,c}$ and $P_{heat,c}$ represent the cooling and heating load under the cooling model (emissivity = 0.92). $P_{cool,h}$ and $P_{heat,h}$ represent the cooling and heating load under the heating model (emissivity = 0.07). The energy consumption per hour for the building was calculated as:

$$E = 3600 \times \mathrm{MAX}(P_{cool}, P_{heat}) \tag{7}$$

Thus, the energy consumption for heating and cooling modes can be calculated as E_h and E_c. Considering the dynamic tuning ability of the device, the building can vary its emissivity in response to the demand. Therefore, the building can use the minimal energy cost among the heating and cooling modes, which can be calculated as:

$$E_d = \mathrm{MIN}(E_h, E_c) \tag{8}$$

The total energy cost all year round was obtained by summing up the hourly energy costs.

DFT calculations

To model the adsorption mechanism on graphene and Pt surface, self-consistent DFT calculations were carried out using the Bayesian error estimation function with van der Waals correlation exchange-correlation functional owing to its accuracy for describing adsorption energies and van der Waals interaction between graphene layers, as implemented in the open-source package GPAW[47–49]. All simulations were carried out with the help of the Python package asebasic (GitHub: https://github.com/kianpu34593/asebasic) developed by Jiankun Pu. Calculator setting convergence tests were conducted on bulk Pt, Cu and pristine monolayer graphene. Real-space grid and *k*-point were considered converged when the difference of energies was within 0.015 eV per atom. The calculator settings are listed in Supplementary Table 2. To set up the slab for adsorption energy, asebasic was used to create, manipulate, visualize and analyse the slab structures. The bottom two layers on the *z*-axis of the Pt slab were held fixed. Periodic boundary conditions were used for the *x* and *y* directions. Dipole correction was turned on, and a vacuum of 10 Å was added along the *z*-axis on both sides of the slab. The minimum number of layers needed for the slab was tested for convergence against the surface energy using asebasic. The convergence criterion was set to be 0.015 eV per atom. Lastly, to carry out the adsorption and interaction simulation, AutoCat (GitHub: https://github.com/aced-differentiate/auto_cat/tree/master) was used to generate all the possible adsorption sites on a slab. Then, asebasic handled the calculation automatically and selected the most stable adsorption energy. All simulations were considered converged for forces <0.01 eV $Å^{-1}$.

To avoid calculating the free energy of solution species, the limiting potential for the adsorption step can be calculated using the computational Cu electrode reference, which is given by

$$\Delta G_{Cu^{2+}} + \Delta G_{2e^-(U=0)} = \Delta G \tag{9}$$

We approximated the free energies to be equal to their DFT energies, neglecting entropic contributions, as

$$E^{\theta}_{ads} = \left(E^{\theta}_{slab} - E^{clean}_{slab}\right) - E^{bulk}_{Cu} \tag{10}$$

where E^{θ}_{slab} is the DFT energy of the substrate with Cu adatom, E^{clean}_{slab} is the DFT energy of the pure substrate and E^{bulk}_{Cu} is the DFT energy of the bulk Cu.

Data availability

All data needed to support the conclusions in the paper are present in the manuscript and/or Supplementary Information. Additional data related to this paper may be requested from the corresponding authors.

Code availability

Codes for DFT simulation are available on GitHub at https://github.com/kianpu34593/asebasic. Custom codes in Matlab and Python used for EMT calculation, building energy saving simulation and post-processing are available upon written request from the corresponding authors.

References

1. Kammen, D. M. & Sunter, D. A. City-integrated renewable energy for urban sustainability. *Science* **352**, 922–928 (2016).
2. Li, T. et al. A radiative cooling structural material. *Science* **364**, 760–763 (2019).
3. Rogelj, J. et al. Energy system transformations for limiting end-of-century warming to below 1.5 °C. *Nat. Clim. Change* **5**, 519–527 (2015).
4. *Heating and Cooling* (Department of Energy, 2013).

5. Li, X. et al. Integration of daytime radiative cooling and solar heating for year-round energy saving in buildings. *Nat. Commun.* **11**, 6101 (2020).
6. Zhou, L. et al. A polydimethylsiloxane-coated metal structure for all-day radiative cooling. *Nat. Sustain.* **2**, 718–724 (2019).
7. Raman, A. P., Anoma, M. A., Zhu, L., Rephaeli, E. & Fan, S. Passive radiative cooling below ambient air temperature under direct sunlight. *Nature* **515**, 540–544 (2014).
8. Hsu, P.-C. et al. Radiative human body cooling by nanoporous polyethylene textile. *Science* **353**, 1019–1023 (2016).
9. Jelle, B. P., Kalnæs, S. E. & Gao, T. Low-emissivity materials for building applications: a state-of-the-art review and future research perspectives. *Energy Build.* **96**, 329–356 (2015).
10. Peng, Y. et al. Coloured low-emissivity films for building envelopes for year-round energy savings. *Nat. Sustain.* **5**, 339–347 (2022).
11. Sherwood, S. C. Adapting to the challenges of warming. *Science* **370**, 782–783 (2020).
12. Li, X., Xie, W., Sui, C. & Hsu, P.-C. Multispectral thermal management designs for net-zero energy buildings. *ACS Mater. Lett.* **2**, 1624–1643 (2020).
13. Wang, S. et al. Thermochromic smart windows with highly regulated radiative cooling and solar transmission. *Nano Energy* **89**, 106440 (2021).
14. Wang, S. et al. Scalable thermochromic smart windows with passive radiative cooling regulation. *Science* **374**, 1501–1504 (2021).
15. Tang, K. et al. Temperature-adaptive radiative coating for all-season household thermal regulation. *Science* **374**, 1504–1509 (2021).
16. Lin, C. et al. All-weather thermochromic windows for synchronous solar and thermal radiation regulation. *Sci. Adv.* **8**, eabn7359 (2022).
17. Zhao, H., Sun, Q., Zhou, J., Deng, X. & Cui, J. Switchable cavitation in silicone coatings for energy-saving cooling and heating. *Adv. Mater.* **32**, 2000870 (2020).
18. Mandal, J. et al. Porous polymers with switchable optical transmittance for optical and thermal regulation. *Joule* **3**, 3088–3099 (2019).
19. Li, M., Liu, D., Cheng, H., Peng, L. & Zu, M. Manipulating metals for adaptive thermal camouflage. *Sci. Adv.* **6**, eaba3494 (2020).
20. Araki, S., Nakamura, K., Kobayashi, K., Tsuboi, A. & Kobayashi, N. Electrochemical optical-modulation device with reversible transformation between transparent, mirror, and black. *Adv. Mater.* **24**, OP122–OP126 (2012).
21. Cai, G. et al. Molecular level assembly for high-performance flexible electrochromic energy-storage devices. *ACS Energy Lett.* **5**, 1159–1166 (2020).
22. Chandrasekhar, P. et al. Variable-emittance infrared electrochromic skins combining unique conducting polymers, ionic liquid electrolytes, microporous polymer membranes, and semiconductor/polymer coatings, for spacecraft thermal control. *J. Appl. Polym. Sci.* https://doi.org/10.1002/app.40850 (2014).
23. Eh, A. L.-S., Chen, J., Zhou, X., Ciou, J.-H. & Lee, P. S. Robust trioptical-state electrochromic energy storage device enabled by reversible metal electrodeposition. *ACS Energy Lett.* **6**, 4328–4335 (2021).
24. Hernandez, T. S. et al. Electrolyte for improved durability of dynamic windows based on reversible metal electrodeposition. *Joule* **4**, 1501–1513 (2020).
25. Li, M., Liu, D., Cheng, H., Peng, L. & Zu, M. Graphene-based reversible metal electrodeposition for dynamic infrared modulation. *J. Mater. Chem. C* **8**, 8538–8545 (2020).
26. Rao, Y. et al. Ultra-wideband transparent conductive electrode for electrochromic synergistic solar and radiative heat management. *ACS Energy Lett.* **6**, 3906–3915 (2021).
27. Salihoglu, O. et al. Graphene-based adaptive thermal camouflage. *Nano Lett.* **18**, 4541–4548 (2018).
28. Strand, M. T. et al. Polymer inhibitors enable >900 cm^2 dynamic windows based on reversible metal electrodeposition with high solar modulation. *Nat. Energy* **6**, 546–554 (2021).
29. Ergoktas, M. S. et al. Multispectral graphene-based electro-optical surfaces with reversible tunability from visible to microwave wavelengths. *Nat. Photon.* **15**, 493–498 (2021).
30. Baechler, M. C. et al. *Building America Best Practices Series: Volume 7.1: Guide to Determining Climate Regions by County* (Pacific Northwest National Laboratory, 2010).
31. Young, J. A. Dimethyl sulfoxide. *J. Chem. Educ.* **85**, 629 (2008).
32. Tao, X. et al. A bistable variable infrared emissivity device based on reversible silver electrodeposition. *Adv. Funct. Mater.* **32**, 2202661 (2022).
33. Reyna, J. et al. *U.S. Building Stock Characterization Study: A National Typology for Decarbonizing U.S. Buildings. Part 1: Residential Buildings* (National Renewable Energy Laboratory, 2021).
34. Moulder, J. F., Stickle, W. F., Sobol, P. E. & Bomben, K. D. *Handbook of X-ray Photoelectron Spectroscopy* (Perkin-Elmer, 1992).
35. Usman, M. S., Ibrahim, N. A., Shameli, K., Zainuddin, N. & Yunus, W. M. Z. W. Copper nanoparticles mediated by chitosan: synthesis and characterization via chemical methods. *Molecules* **17**, 14928–14936 (2012).
36. Eslami, M., Golestani-fard, F., Saghafian, H. & Robin, A. Study on tribological behavior of electrodeposited Cu–Si3N4 composite coatings. *Mater. Des.* **58**, 557–569 (2014).
37. Cai, W. & Shalaev, V. in *Optical Metamaterials* 11–37 (Springer, 2010).
38. Kats, M. A., Blanchard, R., Genevet, P. & Capasso, F. Nanometre optical coatings based on strong interference effects in highly absorbing media. *Nat. Mater.* **12**, 20–24 (2013).
39. Born, M. & Wolf, E. *Principles of Optics: Electromagnetic Theory of Propagation, Interference and Diffraction of Light* (Elsevier, 2013).
40. Jäckle, M. & Groß, A. Microscopic properties of lithium, sodium, and magnesium battery anode materials related to possible dendrite growth. *J. Chem. Phys.* **141**, 174710 (2014).
41. Pande, V. & Viswanathan, V. Computational screening of current collectors for enabling anode-free lithium metal batteries. *ACS Energy Lett.* **4**, 2952–2959 (2019).
42. Wang, X., Tabakman, M. S. & Dai, H. Atomic layer deposition of metal oxides on pristine and functionalized graphene. *J. Am. Chem. Soc.* **130**, 8152–8153 (2008).
43. Kunič, R. Carbon footprint of thermal insulation materials in building envelopes. *Energy Effic.* **10**, 1511–1528 (2017).
44. Tártaro, A. S., Mata, T. M., Martins, A. A. & Esteves da Silva, J. C. G. Carbon footprint of the insulation cork board. *J. Clean. Prod.* **143**, 925–932 (2017).
45. Pal, S. K., Takano, A., Alanne, K. & Siren, K. A life cycle approach to optimizing carbon footprint and costs of a residential building. *Build. Environ.* **123**, 146–162 (2017).
46. Posani, M., Veiga, R. & de Freitas, V. P. Retrofitting historic walls: feasibility of thermal insulation and suitability of thermal mortars. *Heritage* **4**, 2009–2022 (2021).
47. Perdew, J. P., Burke, K. & Ernzerhof, M. Generalized gradient approximation made simple. *Phys. Rev. Lett.* **77**, 3865 (1996).
48. Mortensen, J. J., Hansen, L. B. & Jacobsen, K. W. Real-space grid implementation of the projector augmented wave method. *Phys. Rev. B* **71**, 035109 (2005).

49. Enkovaara, J. et al. Electronic structure calculations with GPAW: a real-space implementation of the projector augmented-wave method. *J. Phys. Condens. Matter* **22**, 253202 (2010).

Acknowledgements

We thank M. D. McGehee and A. L. Yeang (University of Colorado, Boulder, Department of Chemical and Biological Engineering) for the valuable discussion regarding electrodeposition and electrolyte synthesis, G. Tan (Zhejiang University) for kindly helping with the building energy saving calculation, and D. Wang (University of Chicago, Department of Chemistry) for helping with EDX mapping. The project was sponsored by the Collaboration Grants for Climate Change from Nicholas Institute for Energy, Environment & Sustainability and the startup fund by Pratt School of Engineering at Duke University.

Author contributions

P.-C.H. and C.S. conceived the idea. C.S. performed all the experiments, optical fitting, building energy simulation and corresponding data analyses. T.-H.C. helped with the heat transfer measurement. V.V. and J.P. performed the DFT calculation. Y.-T.L., Y.R. and J.L. helped with the transparent electrode fabrication. X.L. helped with the energy saving calculation. Y.H. helped with the SEM and EDX mapping. R.W. and K.W. helped with the hydrophobic treatment and mid-IR transparent pigment spray-coating experiments. C.S., J.P. and P.-C.H. wrote the manuscript with input from all co-authors.

Competing interests

P.-C.H., C.S. and Y.R. have a 2021 US patent application (63/256,136). The other authors declare no competing interests.

Additional information

Supplementary information The online version contains supplementary material available at https://doi.org/10.1038/s41893-022-01023-2.

Correspondence and requests for materials should be addressed to Venkatasubramanian Viswanathan or Po-Chun Hsu.

Peer review information *Nature Sustainability* thanks Yi Long, Junqiao Wu and the other, anonymous, reviewer(s) for their contribution to the peer review of this work.